

# Graphene-based crack lithography for high-throughput fabrication of terahertz metamaterials

Sejeong Won<sup>a</sup>, Hyun-June Jung<sup>a</sup>, Dasom Kim<sup>b</sup>, Sang-Hun Lee<sup>c</sup>, Do Van Lam<sup>d</sup>,  
Hyeon-Don Kim<sup>d</sup>, Kwang-Seop Kim<sup>d,e</sup>, Seung-Mo Lee<sup>d,e</sup>, Minah Seo<sup>c</sup>, Dai-Sik Kim<sup>b</sup>,  
Hak-Joo Lee<sup>a</sup>, Jae-Hyun Kim<sup>d,e,\*</sup>

<sup>a</sup> Center for Advanced Meta-Materials (CAMM), Daejeon, 34103, Republic of Korea

<sup>b</sup> Department of Physics, Ulsan National Institute of Science and Technology (UNIST), Republic of Korea

<sup>c</sup> Sensor System Research Center, Korea Institute of Science and Technology, Seoul, 02792, Republic of Korea

<sup>d</sup> Nano-Convergence Mechanical Systems Research Division, Korea Institute of Machinery & Materials (KIMM), Daejeon, 34103, Republic of Korea

<sup>e</sup> Department of Nano-Mechatronics, Korea University of Science & Technology (UST), 217 Gajeong-ro, Yuseong-gu, Daejeon, 34113, Republic of Korea

## ARTICLE INFO

### Article history:

Received 27 August 2019

Received in revised form

10 October 2019

Accepted 5 November 2019

Available online 11 November 2019

## ABSTRACT

Terahertz (THz) nanoantennas have significant potential for versatile applications in THz spectroscopy because of their capability for strong electromagnetic field localization. Electron-beam lithography or focused ion beam machining is typically employed to fabricate nanoantenna structures. These nano-lithography methods present limitations in the widespread utilization of THz nanoantennas because of their high cost and low productivity. In this work, we proposed graphene-based crack lithography as a high throughput fabrication method for nanoantenna structures. A double-layer graphene interface was introduced to enable independent control of the nanoantenna dimensions and provide graphene-based nanoantenna structures. We analyzed the underlying mechanism of graphene-based cracking and developed an analytical model governing the geometric parameters of the fabricated nanostructures. As a vital application of the fabricated nanoantenna structures, we demonstrated the highly sensitive detection of D-Glucose molecules. Graphene-based crack lithography can provide a cost-effective method for generating nanoantenna structures with the desired characteristics and can accelerate the development of practical applications of electromagnetic metamaterials.

© 2019 Elsevier Ltd. All rights reserved.

## 1. Introduction

Terahertz (THz) spectroscopy has attracted significant attention in chemical and biomedical sensing because of its noninvasive, non-ionizing, and label-free characteristics [1]. These characteristics enable the use of THz spectroscopy in the analysis of chemical substances and biomaterials without the complexities induced by fluorescence tagging or sample pretreatment [2–5]. Notwithstanding this capability, THz spectroscopy has been limited to macroscopic ensembles of material compounds because of its low sensitivity and poor spatial resolution originating from the long THz wavelengths. Metamaterial-based THz spectroscopy has been

developed to overcome this fundamental limitation. Nanoantennas are crucial elements of THz metamaterials and can significantly enhance the THz field with a broad tunability of resonant frequencies [6]. THz sensing with nanoantennas has been introduced to detect small molecules with high sensitivity [7–10]. To be utilized in THz spectroscopy, thousands of nanoantennas should be formed in an area of at least a few mm<sup>2</sup> [7]. However, fabricating the THz nanoantennas usually requires time-consuming and expensive techniques such as E-beam lithography and focused ion beam (FIB) machining [7,11–14]. The necessity for these techniques has limited the widespread utilization of THz metamaterials.

Recently, mechanical deformation of thin-film structures via cracking, wrinkling, and collapsing has been considered as a cost-effective and productive method for creating nanopatterns [15–21]. In particular, the cracking-based approach appears to be the most promising because it can generate nanopatterns over a large-scale substrate at the same time and can be scaled down to

\* Corresponding author. Nano-Convergence Mechanical Systems Research Division, Korea Institute of Machinery & Materials (KIMM), Daejeon, 34103, Republic of Korea.

E-mail address: [jaehkim@kimm.re.kr](mailto:jaehkim@kimm.re.kr) (J.-H. Kim).

the nanometer range [18,19,22,23]. The formation of cracks with dimensions of a few nanometers has been demonstrated, and various nanopatterns generated from cracks have been produced at the wafer scale. The initiation and propagation of cracks have been controlled using the bow type structures, by varying the thickness of thin films or using notch structures [15–19,24–28]. Despite the progress in producing and manipulating cracks, there are some limitations in their application to THz nanoantennas. Most approaches are only applicable to a particular class of materials or have difficulties in independently controlling the dimensions of patterns because a tensile cracking load affects both the width and spacing of the cracks. For nanoantenna applications, conductive materials should be utilized, and the dimensions of nanopatterns such as the width, spacing, and length of the nanorods should be controlled independently to obtain the desired resonant characteristics of THz waves.

In this study, we propose a highly-productive nanoantenna fabrication method using graphene-assisted cracking. A graphene interface is introduced between a thin film and a polymeric substrate to enable independent control of the nanoantenna dimensions. The well-ordered nanoantennas of graphene, metal and graphene nanoslits with metallic rods are generated over a large area by the proposed cracking method, and the underlying mechanism of the cracking is analyzed for the dimensional control of cracks. The highly-sensitive THz detection of D-Glucose is demonstrated using the fabricated THz nanoantennas.

## 2. Experimental

### 2.1. Growth and transfer of graphene onto a polyimide (PI) substrate

Monolayer graphene was synthesized on Cu foil using the CVD process. A 35- $\mu\text{m}$ -thick Cu foil (JX Nippon Mining & Metals Corporation) was used as a catalyst for graphene synthesis and was pre-heated at 400 °C for 60 min with 300 sccm of Ar and 10 sccm of  $\text{H}_2$  at 620 mTorr. It was heat-treated again at 1000 °C under 300 sccm of Ar and 10 sccm of  $\text{H}_2$  at 620 mTorr for 60 min. The growth of graphene was then initiated with the Ar (300 sccm)/ $\text{H}_2$  (10 sccm)/ $\text{CH}_4$  (15 sccm) gas mixture for 15 min at 700 mTorr. After the growth of graphene, the sample was cooled to room temperature with 300 sccm of Ar and 10 sccm of  $\text{H}_2$  at 620 mTorr for 120 min.

Following the growth of graphene, a PET/silicone film was attached to the graphene-grown Cu foil using a laminator. The Cu foil was etched using a 0.1 M ammonium persulfate ( $(\text{NH}_4)_2\text{S}_2\text{O}_8$ , Sigma-Aldrich) solution with 5 mM imidazole ( $\text{C}_3\text{H}_4\text{N}_2$ , Sigma-Aldrich) and 50 mM sulfuric acid ( $\text{H}_2\text{SO}_4$ , Sigma-Aldrich). The PET/silicone/graphene was rinsed with deionized (DI) water for 30 min and dried. Double-layer graphene was transferred to a 25- $\mu\text{m}$ -thick PI substrate by dry transfer using the PET/silicone and a hot roller [29].

Organic residues and metallic contaminations accompany the CVD graphene due to the etching process of metal catalyst and transfer process [30]. Therefore, the PET/silicone film as dispersive adhesion medium was used to reduce the polymer residue [31]. On the other hand, commonly used wet-etching transfer cannot remove metallic impurities from transferred graphene monolayer [32]. To remove the remaining impurities, we need to use additional process such as electrochemical etching [33].

### 2.2. Deposition of $\text{Al}_2\text{O}_3$ on double-layer graphene/PI

The double-layer graphene (DLG)/PI substrate structure was loaded into a thermal ALD chamber (S200, Savannah). The chamber was then evacuated to about 0.1 Torr under a 20 sccm  $\text{N}_2$  flow. The

deposition was carried out at 70 °C using trimethylaluminum ( $\text{Al}(\text{CH}_3)_3$ , TMA, Aldrich) and  $\text{H}_2\text{O}$  as precursors. ALD was set in exposure mode to ensure uniform deposition of  $\text{Al}_2\text{O}_3$ . For each ALD cycle, the  $\text{H}_2\text{O}$  pulse was 0.1 s in duration, with a 20-s exposure, and 30-s purging time. This was followed by a 0.015-s duration, 20-s exposure, and 30-s purging time for the TMA pulse.

### 2.3. Graphene-based crack lithography

#### 2.3.1. Graphene nanoslits

Tensile deformation was applied on the rectangular  $\text{Al}_2\text{O}_3$ /DLG/PI with a width of 10 mm and a gage length of 40 mm using the tensile jig to generate cracks on the alumina film. The exposed graphene under the cracks was removed by  $\text{O}_2$  plasma etching for 15 s at 100 W. Graphene nanoslits were formed by detaching  $\text{Al}_2\text{O}_3$ /upper graphene using the adhesive stamp.

#### 2.3.2. Graphene–metallic nanorods

To fabricate graphene–metallic nanorods, the deposition process of the Au layer was added to the process for fabricating graphene nanoslits. After  $\text{O}_2$  plasma etching of cracked  $\text{Al}_2\text{O}_3$ /DLG/PI, an Au layer with a thickness of 100 nm was deposited on the  $\text{Al}_2\text{O}_3$ /DLG/PI using a shadow mask to control the length parallel to the cracks in the area of the deposited film. The Au layer was deposited on the exposed area of the polymer film as well as the cracked alumina film, and the cracked Au/ $\text{Al}_2\text{O}_3$ /upper graphene was then detached using the adhesive stamp. As a result, Au nanorods with lower graphene nanoslits are formed on the PI substrate.

#### 2.3.3. Metallic nanorods

Au nanorods were formed by removing the graphene from the graphene–metallic nanorods by performing additional  $\text{O}_2$  plasma etching for 50 s at 100 W.

#### 2.3.4. Metallic nanoslots

Cu nanorods with a thickness of 50 nm were formed using the Cu material in the process of metallic nanorods. An Au layer with a thickness of 100 nm was deposited on the Cu nanorods. Au nanoslots were fabricated by removing the Cu nanorods using Cu etchant with sonication for 5 min. The Au nanoslots were rinsed using DI water for 1 min and dried.

### 2.4. Tensile test with in-situ optical microscopy measurements

Rectangular  $\text{Al}_2\text{O}_3$ /DLG/PI with a width of 10 mm and a gage length of 40 mm was used for the tensile test. In-situ optical microscopic observation was carried out during the uniaxial tensile test to study the generation and propagation of cracks of the  $\text{Al}_2\text{O}_3$  layers. This observation enabled the quantitative measurement of the cracks at a variety of applied strains without any release of the strain. The crack density is defined as the total length of the cracks per unit area [34,35].

### 2.5. THz time-domain spectroscopy measurement

The THz transmission spectrum in the frequency range from 0.2 to 2.5 THz was acquired using a commercial THz time-domain spectroscopy system (Zomega Z-3XL). The system was operated based on a Ti: Sapphire pulsed laser with an 800-nm central wavelength, 100-fs pulse width, and 80-MHz repetition rate. The laser beam was divided into two parts inside the THz system for emission using a photoconductive antenna and detection using the electro-optic sampling method. The THz waves were focused onto the sample on the square metal hole (2.0 mm  $\times$  2.0 mm) of the sample holder by a pair of TPX (polymethylpentene) lenses. The

THz transmittance of the sample is defined as  $T(\omega) = T_{sam}(\omega)/T_{ref}(\omega) = |E_{sam}(\omega)|^2/|E_{ref}(\omega)|^2$ , where  $E_{sam}$  and  $E_{ref}$  are the transmitted electric fields through the sample and the bare substrate, respectively. For sensing applications, optimization of the nanoslot antennas to the absorption resonance of the target material is crucial. Thus, the absorption spectrum of the glucose in pellet form was measured. Well-ground glucose powder using a mortar was pressed in a pellet die under 2000 psi for 5 min. The diameter and thickness of the pellet were 8 mm and 460  $\mu\text{m}$ , respectively. The absorption spectrum was measured after mounting the pellet on the sample holder. Sensitive detection of the D-glucose molecule using the nanoslot antennas was demonstrated as shown in the process of Fig. S1. Aqueous solutions were prepared by dissolving D-Glucose molecules in DI water with a concentration of 3 mg/ml, and a 4- $\mu\text{L}$  solution was then dropped onto a 2 mm  $\times$  2 mm area of both the nanoslot antennas and bare substrate. The THz transmittance spectrum was measured after drying the samples at room temperature for 1 h to remove the water absorption signal.

### 3. Result and discussion

#### 3.1. Graphene-based crack lithography for nanostructure fabrication

Fig. 1 illustrates the process of graphene-based crack

lithography. A flexible polymeric substrate was coated with double-layer graphene (DLG) by dry transfer, and an alumina thin film was deposited on the graphene by atomic layer deposition (Fig. 1a). When a tensile force was applied on the rectangular alumina/DLG/substrate using the customized tensile jig, interlayer sliding between the two graphene layers occurred due to small interaction force [29], and ordered cracks were generated in the alumina film (Fig. 1b). At that time, the upper layer of the double-layer graphene was torn together with the alumina film, while the lower graphene layer remained intact and became exposed to air on the cracked regions. The exposed graphene was then removed by  $\text{O}_2$  plasma etching (Fig. 1c). The cracked alumina film with the upper graphene layer was removed by the sticky stamp consisting of polymer film coated with a silicone adhesive layer, and the lower graphene remained on the polymeric substrate. This is because of the low adhesion between the two graphene layers. The resulting structures are called graphene nanoslits (Fig. 1d–1).

For fabricating other structures, a metal layer was selectively deposited using a shadow mask for length control of metal patterns on the strained structure before detaching the cracked alumina thin film (Figs. 1d–2). The metal was deposited on the alumina film and the exposed area of the polymeric substrate. The metal/alumina/upper graphene was detached using the sticky stamp, and the remaining structures of the metal/lower graphene/polymeric substrate are called graphene-metallic nanorods (Fig. 1e).

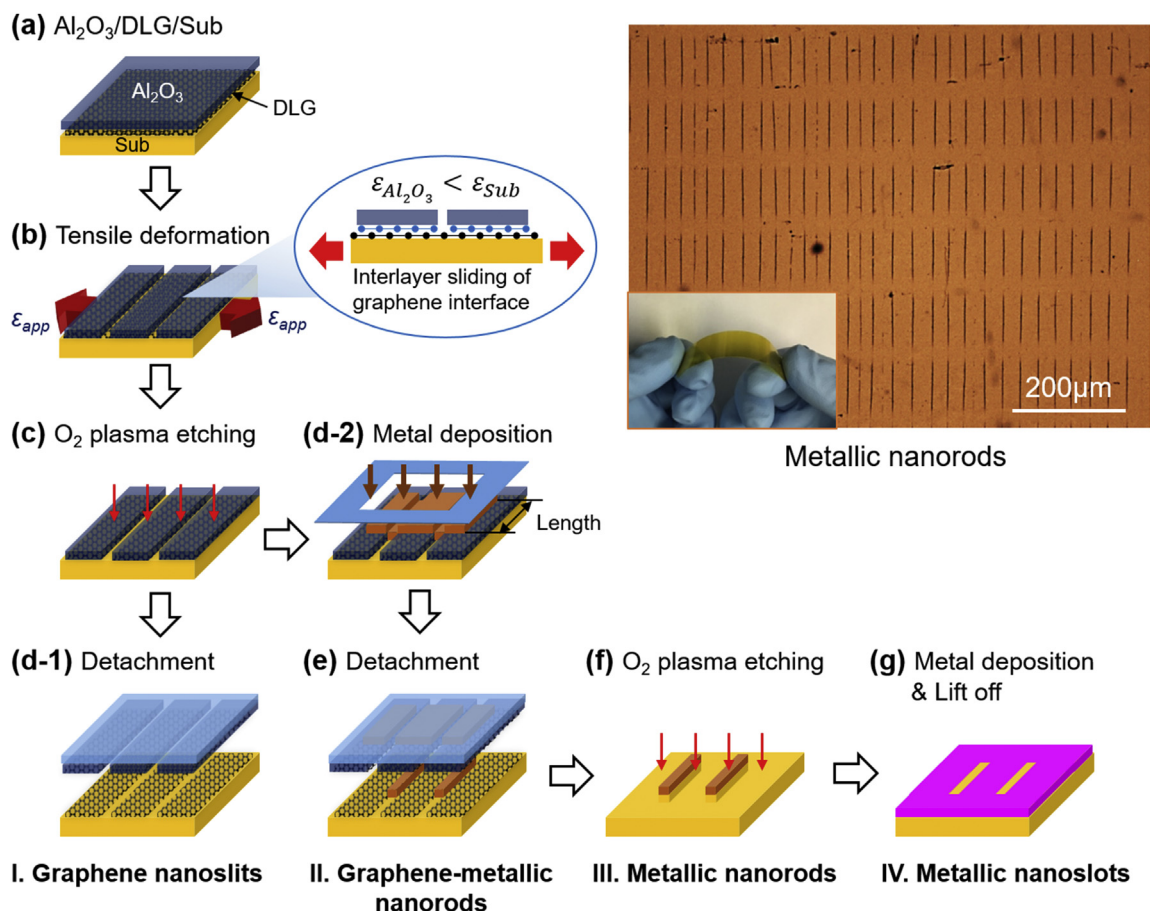


**Fig. 1. Schematic of graphene-based crack lithography for nanostructures.** (a) Deposition of alumina thin film on the transferred double-layer graphene on a flexible polymeric substrate. (b) Cracking of the alumina thin film by applying tensile deformation to the polymeric substrate. (c) Removal of the exposed, lower graphene by  $\text{O}_2$  plasma etching. (d-1) Graphene nanoslits as a first structure after detaching of the cracked  $\text{Al}_2\text{O}_3$ /upper graphene. (d-2) Deposition of metal using a shadow mask for length control of metal patterns. (e) Graphene nanoslits combined with metallic nanorods as a second structure after detaching the upper part. (f) Metallic nanorods as a third structure after removing graphene nanoslits of graphene-metallic nanorods. (g) Metallic nanoslots as a final structure after metal deposition and lift-off process on metallic nanorods. Upper right: photo and optical microscope image of the fabricated metallic nanorods. (A colour version of this figure can be viewed online.)



Furthermore, metallic nanorods were fabricated by removing the graphene layer from the graphene–metallic nanorods using O<sub>2</sub> plasma etching (Fig. 1f). Finally, the metallic nanoslots were fabricated by additional deposition of a metallic layer and using the subsequent lift-off process starting from the nanorods (Fig. 1g, Fig. S2). To summarize, several types of nanostructures (graphene nanoslits, graphene–metallic nanorods, metallic nanorods, and metallic nanoslots) were successfully produced by the proposed graphene-based crack lithography. The upper right corner of Fig. 1 shows macroscopic and optical microscope images of the metallic nanorods.

Fig. 2 shows scanning electron microscopy (SEM) images of the fabricated nanostructures. The left images show arrays of the nanostructures, while the right images show magnified top and cross-sectional images of the marked areas in the left images. To obtain cross-sectional SEM images of the nanostructures, Pt was deposited on the samples to protect them from the focused ion beam and focused ion beam milling was then performed on the samples. The graphene nanoslits have an array of long nano-rectangular apertures made of graphene. In the graphene–metallic nanorods, Au nanorod arrays were formed with a graphene nanoslit layer. In the metallic nanorods, Au nanorod arrays were formed and the surface of the polymeric substrate was etched down by approximately 100 nm during the plasma etching of the graphene layer. The metallic nanoslots have an array of nano-rectangular apertures made of a thin Au layer. AFM analysis was performed to verify the existence of graphene in the graphene nanoslits and the graphene–nanorods (Fig. S3). In the graphene

nanoslits, the graphene layer is transferred on the surface of the PI substrate and the substrate is exposed in the slit area where the graphene has been removed. In graphene–metallic nanorods, Au nanorods are imaged together with the wrinkled graphene layer. In case of metallic nanorods and metallic nanoslots, the graphene layer is not detected. Furthermore, significant lower friction of the graphene nanoslits and the graphene–metallic nanorods than that of the PI substrate indicates that there is a graphene layer on the structures (Fig. S4).

### 3.2. Controlling dimensional parameters of the nanostructures

Since the nanostructures are fabricated from the crack templates, the nanostructures are expected to be formed according to the characteristics of the cracks. Therefore, we conducted an *in-situ* tensile test with optical microscopy measurements to observe the crack characteristics in the multilayer structures with the graphene interface. Fig. 3a shows the variation in crack density with respect to the applied tensile strain depending on the thickness of the alumina film. The cracks occur initially at a strain of about 0.4%, and the crack density rapidly increases before becoming saturated at a strain of about 1%. Saturated crack density depends on the thickness of the alumina. When there is a graphene interface, the strain at which the crack density is saturated is greatly reduced [29]. These small saturated strains can be explained by the interlayer sliding of the graphene interface. The graphene interface relaxes the tensile stress that is transferred from the polymeric substrate to the thin film, which prevents further cracking [36,37]. As the tensile

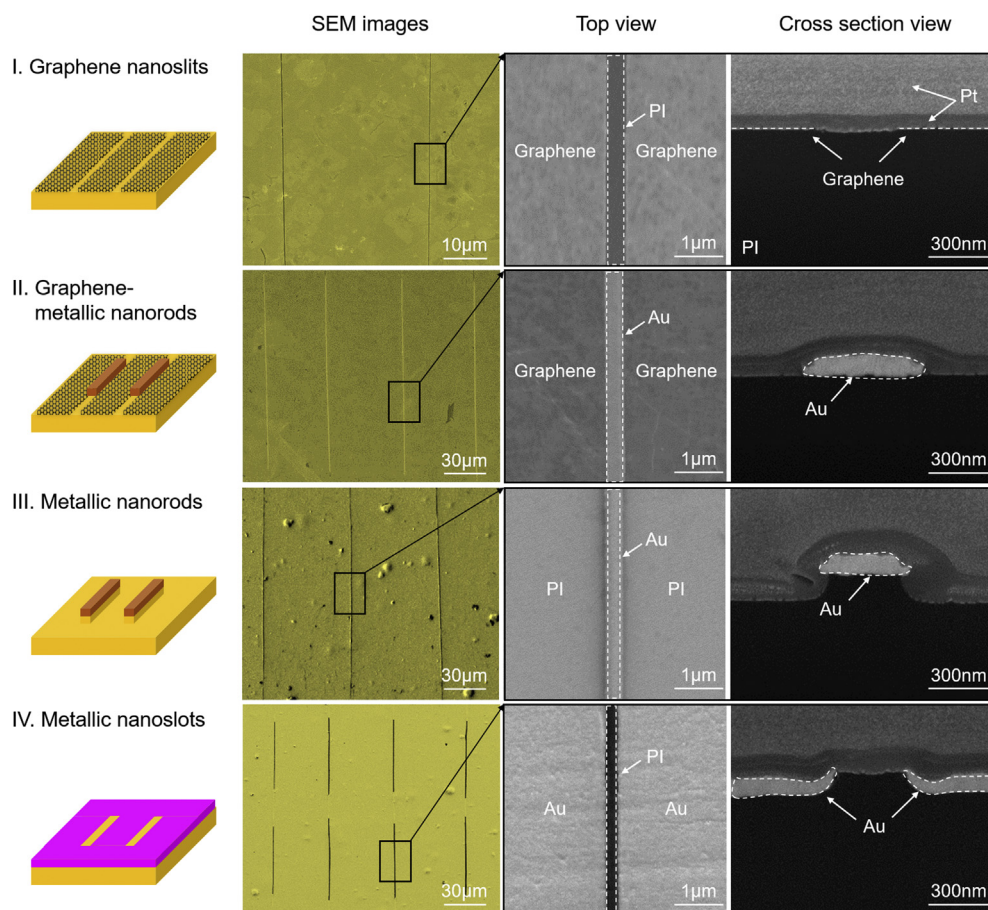
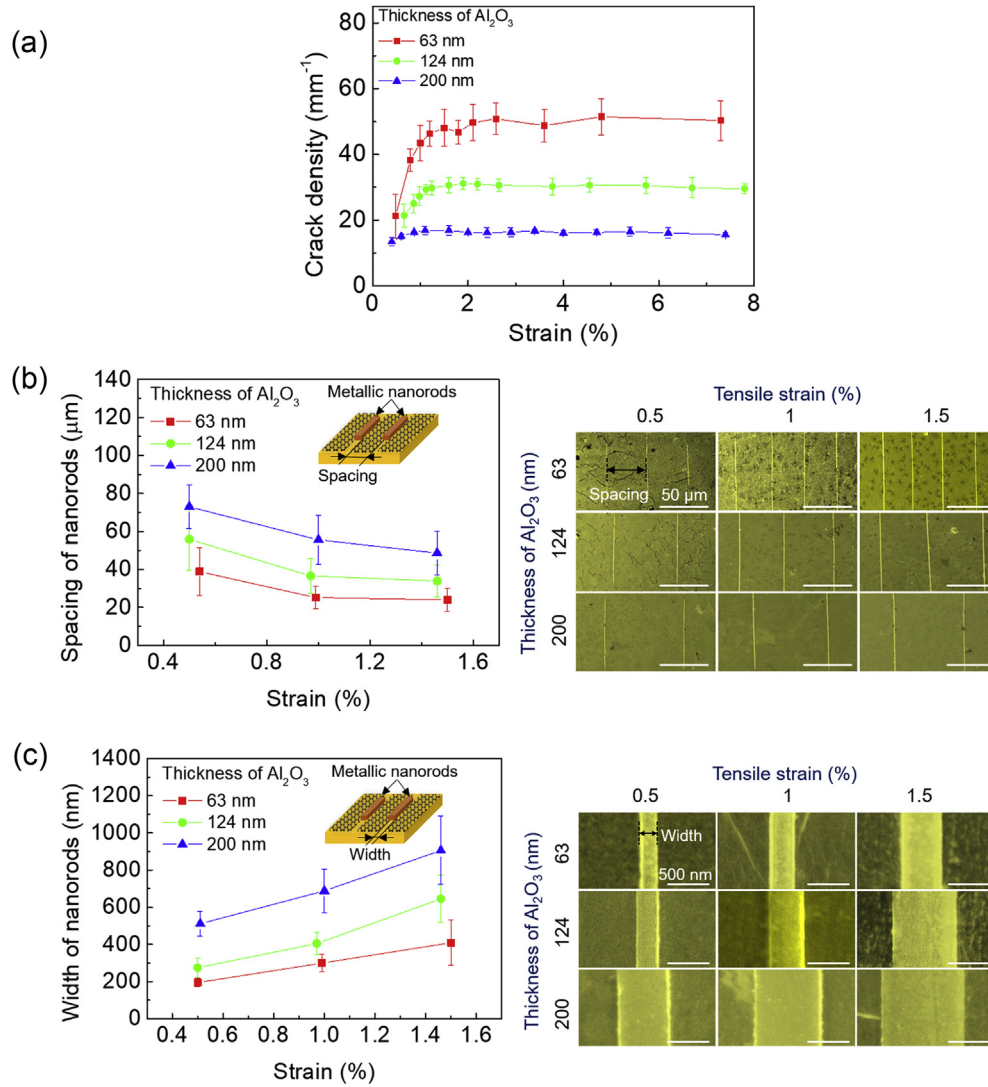


Fig. 2. Characterization of the nanostructures. SEM images of graphene nanoslits, graphene–metallic nanorods, metallic nanorods, and metallic nanoslots. Left: Images of nanostructure arrays, Right: Magnified top and cross-sectional images of the marked areas in the left images. (A colour version of this figure can be viewed online.)



**Fig. 3. Controllable dimensional parameters of nanostructures** (a) *In-situ* tensile test results of  $\text{Al}_2\text{O}_3/\text{DLG}/\text{PI}$ . (b) The spacing between two adjacent metallic nanorods with respect to tensile strain by varying the alumina thin film thickness. (c) Width of metallic nanorods with respect to tensile strain by varying the alumina thin film thickness. (A colour version of this figure can be viewed online.)

strain increases, the width of the cracks, rather than the density, increases. The alumina thickness affects the crack density such that the thicker the alumina, the lower the crack density. To sum up, crack width and density depend on tensile strains and the thickness of alumina, respectively because graphene interface makes crack density saturated at small strains. Therefore, dimensional parameters of cracks can be controlled independently by the graphene interface.

To check how the nanostructures were affected by alumina thickness and tensile strain, width and spacing of metallic nanorods in the graphene-metallic nanorods were analyzed. As can be seen in Fig. 3b, the spacing of metallic nanorods decreases and saturates with the tensile strain. The saturated spacing of metallic nanorods is proportional to the thickness of the alumina film. Fig. 3c shows the width of the metallic nanorods according to the tensile strain by varying the thickness of the alumina film. The width of the metallic nanorods increases with the alumina thickness, and the width increases with the strain when the thickness of the alumina is constant. Nanostructures were also found to have the same characteristics as cracks.

### 3.3. Analysis of graphene-based cracking using an elastic-plastic shear lag model

A shear lag model that describes stress transfer by interfacial shear stress was adopted to understand the behavior of cracks in the multilayer structures. We utilized the elastic-plastic shear lag model to analyze the effect of the graphene interlayer, as illustrated in the schematic of Fig. 4a [38]. In this model, the crack density  $n$  can be expressed as a function of the strain, as follows:

$$n = \frac{G\gamma_p}{2Eq} \left[ [\epsilon_i - \epsilon] \cosh \left[ \sinh^{-1} \left[ \frac{\gamma_p \sqrt{t_r M_r}}{\epsilon - \epsilon_i} \right] \right] + \epsilon \right. \\ \left. + \gamma_p \sqrt{t_r M_r} \sinh^{-1} \left[ \frac{\gamma_p \sqrt{t_r M_r}}{\epsilon - \epsilon_i} \right] \right]^{-1} \quad (1)$$

Here,  $G$  is the shear modulus of the graphene layers,  $\gamma_p$  is the plastic onset shear strain of the graphene layers,  $E$  is the elastic modulus of the alumina thin film, and  $\epsilon_i = \sigma^*/E$  is the crack onset strain of the alumina layer where  $\sigma^*$  is the effective tensile strength of the alumina thin film. The applied strain is denoted by  $\epsilon$ ,  $t_r = p/q$

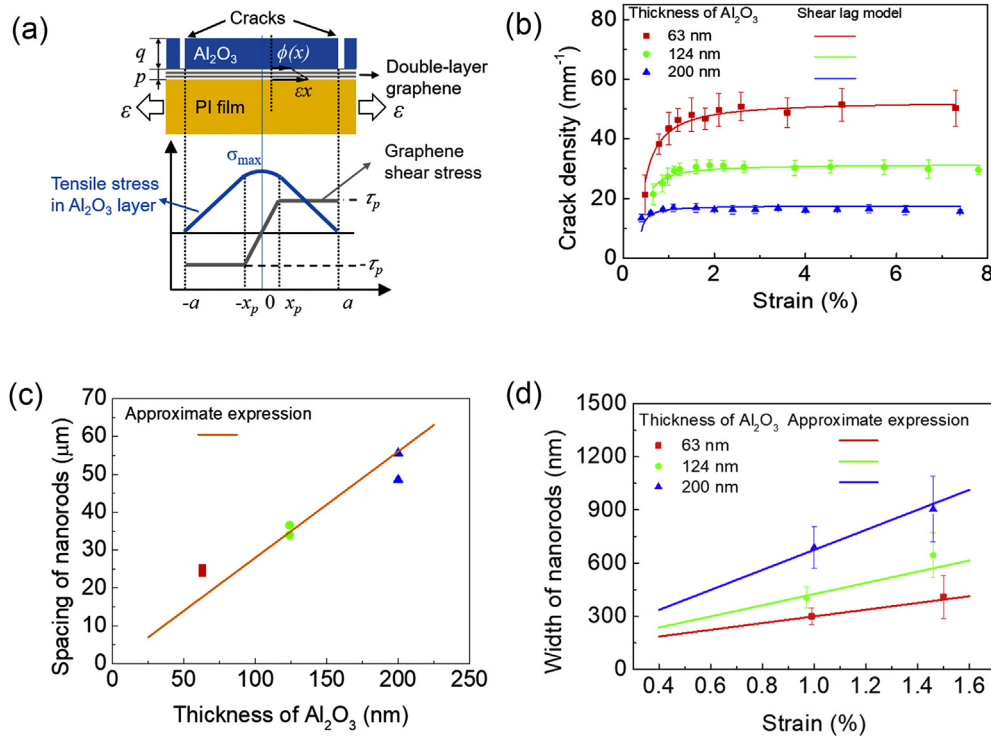


**Fig. 4.** Analysis of graphene-based cracking using an analytical model. (a) Schematic of the elastic-plastic shear lag model. (b) *In-situ* tensile test results of  $\text{Al}_2\text{O}_3/\text{DLG}/\text{PI}$  and the results of the shear lag model. (c) Simplified equation of crack spacing and the spacing of metallic nanorods according to the thickness of the alumina layer. (d) Simplified equation of crack width and metallic nanorods width according to the thickness of the alumina layer and tensile strain. (A colour version of this figure can be viewed online.)

is the thickness ratio of the graphene interface and the alumina thin film where  $p$  is the thickness of the graphene interface, and  $q$  is the thickness of the alumina layer, and  $M_r = G/E$  is the ratio of the shear modulus of the graphene interface to the elastic modulus of the alumina thin film.

In Fig. 4b, the results of the model are compared to the experimental data of crack density. The measured parameters are  $n$ ,  $q$ , and  $\varepsilon$ . The thickness of the graphene interface  $p$  was obtained by doubling the thickness of a single layer of graphene. The parameters to be fitted using the model are  $\gamma_p$ ,  $G/E$  and  $\varepsilon_i = \sigma^*/E$ . Table S1 lists the parameters that were fitted to the shear lag model. The correlation coefficient is 0.98, indicating that the model and test results agree well. As crack spacing is the reciprocal of crack density, this model allows the design of a multilayer structure with a graphene interface with a specific crack spacing. The shear lag model was simplified and the equation for crack spacing ( $S$ ) was obtained as follows (see Supplementary Information S1 for details):

$$S = \frac{2\sigma^*q}{G\gamma_p} \quad (2)$$

This simplified equation shows that the saturated crack spacing is proportional to the thickness and effective tensile strength of alumina and is inversely proportional to the shear modulus and the plastic onset strain of the graphene layers. Meanwhile, strain energy by tensile deformation increases the overall area of the cracks by widening or generating more cracks. Assuming that the area increased by the tensile deformation is equal to the area of the total cracks, the crack width ( $w$ ) can be expressed as

$$w = \frac{2\sigma^*q\varepsilon}{G\gamma_p} = S\varepsilon \quad (3)$$

The simplified equation of crack width indicates that the crack

width can be controlled by changing the tensile strain when the crack spacing has a certain value. Fig. 4c shows that the saturated spacing of metallic nanorods can be described by Equation (2). Characteristics of the width are described well by Equation (3), as shown in Fig. 4d. As the broadening of the fabricated structures occurs in the shadow-mask approach [39], the approximated value of the width of the crack was added to the difference in width between the crack and the metallic nanorods made using the crack template. Therefore, we can see that the spacing and width of cracks can be adjusted using several physical parameters.

### 3.4. THz time-domain spectroscopy results of nanostructures

Antenna dimensions such as width, spacing, and length are important parameters for THz transmittance. The field enhancement increases with the decrease in width of the antennas because the THz field is strongly localized and enhanced by antenna structures [13], and the behavior of the electromagnetic coupling between antennas depends on the spacing of the antennas [40]. Furthermore, the resonant wavelength of the antennas satisfies the condition  $\lambda_{\text{eff}} = 2n_{\text{eff}}l$ , where  $n_{\text{eff}}$  and  $l$  are the effective index of refraction of the antenna-substrate composite and the length of the antennas, respectively [41,42]. Therefore, control of the dimensional parameters of the antenna structures was required to obtain the desired characteristics of THz transmittance. As shown in Fig. S5, THz time-domain spectroscopy was used to verify the performance of the fabricated nanostructures as THz antennas. Among the fabricated structures, graphene or graphene hybrid nanostructures have been usually studied as active metamaterials, where the external electric voltage-induced doping of graphene contributes to the modulation ability [43,44]. Because the effect of graphene in the THz sensing application beyond the scope of this study, graphene nanostructures such as graphene nanoslits and



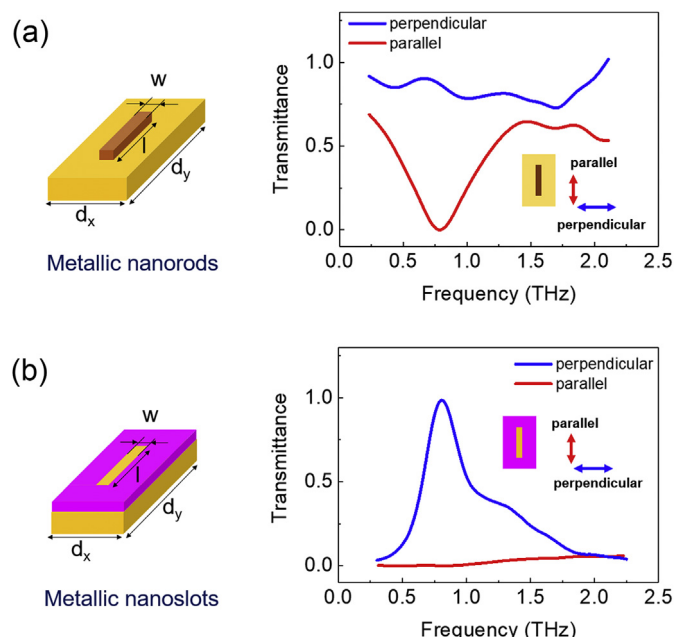


**Fig. 5.** THz transmission spectra of nanostructures. (a) Left: Schematic of the metallic nanorods. Right: THz transmittance of the metallic nanorods.  $w = 512 \text{ nm}$ ,  $l = 100 \text{ }\mu\text{m}$ ,  $d_x = 52 \text{ }\mu\text{m}$ ,  $d_y = 140 \text{ }\mu\text{m}$ . (b) Left: Schematic of the metallic nanoslots. Right: THz transmittance of the metallic nanoslots.  $w = 521 \text{ nm}$ ,  $l = 98 \text{ }\mu\text{m}$ ,  $d_x = 43 \text{ }\mu\text{m}$ ,  $d_y = 138 \text{ }\mu\text{m}$ . (A colour version of this figure can be viewed online.)

graphene–metallic nanorods were excluded from the measurements of THz transmittance. Fig. 5 shows the THz transmittances of metallic nanorods and metallic nanoslots under two different incident polarizations: parallel and perpendicular to the slot direction. Here, the THz transmittance of the structure is defined as  $T_s(\omega) = |E_s(\omega)|^2 / |E_{ref}(\omega)|^2$ , where  $E_s$  and  $E_{ref}$  are the transmitted THz fields through the fabricated structure and a bare substrate, respectively [9]. The transmittance of the fabricated nanostructures is normalized to resonance transmission to clarify THz sensing performance by the field enhancement effect. For the metallic nanorods shown in Fig. 5a, the THz wave mostly penetrates under perpendicular polarization, and a transmission dip at 0.8 THz is observed under parallel polarization. The metallic nanorods exhibit the characteristics of a THz nanoantenna with a polarization extinction ratio of 18.84 dB. For the metallic nanoslots shown in Fig. 5b, the transmittance is close to zero under parallel polarization, while it is maximum at 0.8 THz under perpendicular polarization. The metallic nanoslots exhibit the characteristics of a THz nanoslot antenna with a polarization extinction ratio of 30.62 dB. We found that the metallic nanorods and metallic nanoslots

functioned as high-performance THz nanoantenna structures.

### 3.5. Nanoslot antennas for THz sensing of D-Glucose

A trace of a target molecule can be detected using a THz spectroscopy system assisted by THz nanoantenna structures. We performed measurements of D-Glucose, which is used as an energy source within living organisms, to demonstrate the sensitive detection of the target molecule using the nanoslot antennas. The D-Glucose molecule has a strong absorption peak at 1.4 THz, as can be seen in Fig. 6a [7]. Nanoslot antennas with resonant frequencies of 1.4 THz were fabricated. The average length and width of the antennas were  $59.5 \text{ }\mu\text{m}$  and  $521 \text{ nm}$ , respectively. The enhancement factor of the antennas was found to be 37.2, which is similar to antennas made with conventional nanolithography [7,14]. When the D-Glucose samples were applied on the glucose-targeted nanoslot antennas, the resonance frequency wasn't shifted toward a lower frequency. This is because the inside of the slot was filled with a polymeric substrate and so the effective refractive index around the slot changed little. However, THz transmittance decreased by 24% at the resonance frequency while there was a negligible reduction in transmittance by D-Glucose samples on bare substrates without nanoslot antennas (Fig. S6a). This demonstrates the highly sensitive detection of D-Glucose using the glucose target antennas. The reason for this sensitive detection is that the absorption area of the detection molecule increased significantly because of the strong localization and enhancement of the THz electric field by the nanoslot antennas [7,14]. Furthermore, when nanoslot antennas that were not targeted at D-Glucose were applied, that is, when the resonant frequency of the nanoslot antennas did not match the absorption peak of D-Glucose, the variation in transmittance was negligible in comparison to the resonance-matched result (Fig. S6b). In short, the produced THz nanoslot antennas demonstrated high sensitivity of THz detection for D-Glucose.

## 4. Conclusion

In this study, we proposed graphene-based crack lithography as a high-throughput fabrication method for THz nanoantenna structures. Several unique nanostructures were fabricated using the graphene interface, which enabled independent control of nanoantenna dimensions and provided graphene-based nanostructures. We also analyzed the underlying mechanism for graphene-based cracking and developed an analytical model for predicting the geometric parameters of the nanostructures fabricated by crack lithography. Based on the analytical model, we can efficiently design and generate THz nanoantenna structures with a targeted operating frequency and a high enhancement factor. As an inspiring

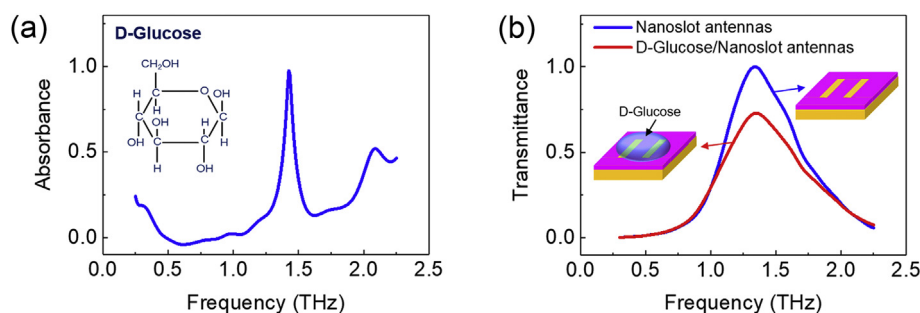


**Fig. 6.** THz measurements for glucose with nanoslot antennas. (a) Absorption spectra of glucose. (b) THz spectra measured for the glucose target nanoslot antennas and D-Glucose on the same nanoslot antennas. (A colour version of this figure can be viewed online.)

application of the fabricated THz nanoantenna structures, we also realized the highly sensitive detection of D-Glucose molecules, which is an essential indicator for biological and medical purposes. The proposed method is a cost-effective fabrication route for THz nanoantenna structures over conventional nanoscale techniques such as E-beam and FIB lithography, which has been an obstacle to the commercialization of THz nanoantenna structures because of its low effectiveness and high fabrication cost.

### Declaration of competing interest

The authors declare that they have no known competing financial interests or personal relationships that could have appeared to influence the work reported in this paper.

### Acknowledgments

This research was supported by the Center for Advanced Materials (CAMP) funded by the Ministry of Science, ICT and the Future Planning as Global Frontier Project (CAMP-No. 2014063700 and 2014063701 and 2019M3A6B3030638), internal research program of KIMM(NK218C) and the National Research Foundation of Korea (NRF) grant funded by the Korea government (MSIT: NRF-2015R1A3A2031768).

### Appendix A. Supplementary data

Supplementary data to this article can be found online at <https://doi.org/10.1016/j.carbon.2019.11.018>.

### References

- [1] W. Xu, L. Xie, Y. Ying, Mechanisms and applications of terahertz metamaterial sensing: a review, *Nanoscale* 9 (2017) 13864–13878.
- [2] K. Meng, T.-N. Chen, T. Chen, L.-G. Zhu, Q. Liu, Z. Li, et al., Terahertz pulsed spectroscopy of paraffin-embedded brain glioma, *J. Biomed. Opt.* 19 (2014), 077001.
- [3] K. Shiraga, Y. Ogawa, T. Suzuki, N. Kondo, A. Irisawa, M. Imamura, Characterization of dielectric responses of human cancer cells in the terahertz region, *J. Infrared, Millim. Terahertz Waves* 35 (2014) 493–502.
- [4] M. Tonouchi, Cutting-edge terahertz technology, *Nat. Photonics* 1 (2007) 97–105.
- [5] B. Fischer, M. Hoffmann, H. Helm, G. Modjesch, P.U. Jepsen, Chemical recognition in terahertz time-domain spectroscopy and imaging, *Semicond. Sci. Technol.* 20 (2005) S246–S253.
- [6] J.H. Kang, J.-H. Choe, D.S. Kim, Q.-H. Park, Substrate effect on aperture resonances in a thin metal film, *Opt. Express* 17 (2009) 15652–15658.
- [7] D.-K. Lee, J.-H. Kang, J.-S. Lee, H.-S. Kim, C. Kim, J.H. Kim, et al., Highly sensitive and selective sugar detection by terahertz nano-antennas, *Sci. Rep.* 5 (2015), 15459.
- [8] A. Toma, S. Tuccio, M. Prato, F.D. Donato, A. Perucchi, P.D. Pietro, et al., Squeezing terahertz light into nanovolumes: nanoantenna enhanced terahertz spectroscopy (NETS) of semiconductor quantum dots, *Nano Lett.* 15 (2015) 386–391.
- [9] C. Lim, S.-H. Lee, Y. Jung, J.-H. Son, J.-H. Choe, Y.J. Kim, et al., Broadband characterization of charge carrier transfer of hybrid graphene-deoxyribonucleic acid junctions, *Carbon* 130 (2018) 525–531.
- [10] D.-K. Lee, J.-H. Kang, J. Kwon, J.-S. Lee, S. Lee, D.H. Woo, et al., Nano metamaterials for ultrasensitive terahertz biosensing, *Sci. Rep.* 7 (2017) 8146.
- [11] M. Seo, J. Kyoung, H. Park, S. Koo, H.-S. Kim, H. Bernien, et al., Active terahertz nanoantennas based on VO<sub>2</sub> phase transition, *Nano Lett.* 10 (2010) 2064–2068.
- [12] H.-R. Park, K.J. Ahn, S. Han, Y.-M. Bahk, N. Park, D.-S. Kim, Colossal absorption of molecules inside single terahertz nanoantennas, *Nano Lett.* 13 (2013) 1782–1786.
- [13] M.A. Seo, H.R. Park, S.M. Koo, D.J. Park, J.H. Kang, O.K. Suwal, et al., Terahertz field enhancement by a metallic nano slit operating beyond the skin-depth limit, *Nat. Photonics* 3 (2009) 152–156.
- [14] S.-H. Lee, D.-K. Lee, C. Kim, Y.M. Jhon, J.-H. Son, M. Seo, Terahertz transmission control using polarization-independent metamaterials, *Opt. Express* 25 (2017) 11436–11443.
- [15] M. Kim, D.-J. Kim, D. Ha, T. Kim, Cracking-assisted fabrication of nanoscale patterns for micro/nanotechnological applications, *Nanoscale* 8 (2016) 9461–9479.
- [16] D. Ha, J. Hong, H. Shin, T. Kim, Unconventional micro-/nanofabrication technologies for hybrid-scale lab-on-a-chip, *Lab Chip* 16 (2016) 4296–4312.
- [17] D. Huh, K.L. Mills, X. Zhu, M.A. Burns, M.D. Thouless, S. Takayama, Tuneable elastomeric nanochannels for nanofluidic manipulation, *Nat. Mater.* 6 (2007) 424–428.
- [18] K.H. Nam, I.H. Park, S.H. Ko, Patterning by controlled cracking, *Nature* 485 (2012) 221–224.
- [19] M. Kim, D. Ha, T. Kim, Cracking-assisted photolithography for mixed-scale patterning and nanofluidic applications, *Nat. Commun.* 6 (2015) 6247.
- [20] M. Nania, F. Foglia, O.K. Matar, J.T. Cabral, Sub-100 nm wrinkling of polydimethylsiloxane by double frontal oxidation, *Nanoscale* 9 (2017) 2030–2037.
- [21] S.-M. Park, Y.S. Huh, H.G. Craighead, D. Erickson, A method for nanofluidic device prototyping using elastomeric collapse, *Proc. Natl. Acad. Sci. U.S.A.* 106 (2009) 15549–15554.
- [22] V. Dubois, F. Niklaus, G. Stemme, Crack-defined electronic nanogaps, *Adv. Mater.* 28 (2016) 2178–2182.
- [23] A. Enrico, V. Dubois, F. Niklaus, G. Stemme, Scalable manufacturing of single nanowire devices using crack-defined shadow mask lithography, *ACS Appl. Mater. Interfaces* 11 (2019) 8217–8226.
- [24] S. Jebil, M. Elbahri, G. Titazu, K. Subannajui, S. Essa, F. Niebelschütz, et al., Integration of thin-film-fracture-based nanowires into microchip fabrication, *Small* 4 (2008) 2214–2221.
- [25] A.T. Skjeltorp, P. Meakin, Fracture in microsphere monolayers studied by experiment and computer simulation, *Nature* 335 (1988) 424–426.
- [26] M. Kim, T. Kim, Crack-photolithography for membrane-free diffusion-based micro/nanofluidic devices, *Anal. Chem.* 87 (2015) 11215–11223.
- [27] B.C. Kim, P. Weerappuli, M.D. Thouless, S. Takayama, Fracture fabrication of a multi-scale channel device that efficiently captures and linearizes DNA from dilute solutions, *Lab Chip* 15 (2015) 1329–1334.
- [28] R. Adelung, O.C. Aktas, J. Franc, A. Biswas, R. Kunz, M. Elbahri, et al., Strain-controlled growth of nanowires within thin-film cracks, *Nat. Mater.* 3 (2004) 375–379.
- [29] S. Won, D.V. Lam, J.Y. Lee, H.-J. Jung, M. Hur, K.-S. Kim, et al., Graphene-based stretchable and transparent moisture barrier, *Nanotechnology* 29 (2018), 125705.
- [30] L.J.A. Macedo, R.M. Iost, A. Hassan, K. Balasubramanian, F.N. Crespihlo, Bio-electronics and interfaces using monolayer graphene, *ChemElectroChem* 6 (2019) 31–59.
- [31] S. Chae, K.H. Cho, S. Won, A. Yi, J. Choi, H.H. Lee, et al., Favorable face-on orientation of a conjugated polymer on roll-to-roll-transferred graphene interface, *Adv. Mater. Interfaces* 4 (2017), 171099.
- [32] G. Lupina, J. Kitzmann, I. Costina, M. Lukosius, C. Wenger, A. Wolff, et al., Residual metallic contamination of transferred chemical vapor deposited graphene, *ACS Nano* 9 (2015) 4776–4785.
- [33] R.M. Iost, F.N. Crespihlo, L. Zuccaro, H.K. Yu, A.M. Wodtke, K. Kern, et al., Enhancing the electrochemical and electronic performance of CVD-grown graphene by minimizing trace metal impurities, *ChemElectroChem* 1 (2014) 2070–2074.
- [34] X.F. Zhu, B. Zhang, J. Gao, G.P. Zhang, Evaluation of the crack-initiation strain of a Cu-Ni multilayer on a flexible substrate, *Scr. Mater.* 60 (2009) 178–181.
- [35] R.M. Niu, G. Liu, C. Wang, G. Zhang, X.D. Ding, J. Sun, Thickness dependent critical strain in submicron Cu films adherent to polymer substrate, *Appl. Phys. Lett.* 90 (2007), 161907.
- [36] S.-H. Jen, J.A. Bertrand, S.M. George, Critical tensile and compressive strains for cracking of Al<sub>2</sub>O<sub>3</sub> films grown by atomic layer deposition, *J. Appl. Phys.* 109 (2011), 084305.
- [37] C. Peng, Z. Jia, D. Bianculli, T. Li, J. Lou, *In situ* electro-mechanical experiments and mechanics modeling of tensile cracking in indium tin oxide thin films on polyimide substrates, *J. Appl. Phys.* 109 (2011), 103530.
- [38] A.P. McGuigan, G.A.D. Griggs, V.M. Burlakov, M. Yanaka, Y. Tsukahara, An elastic-plastic shear lag model for fracture of layered coatings, *Thin Solid Films* 424 (2003) 219–223.
- [39] M.M. Deshmukh, D.C. Ralph, M. Thomas, J. Silcox, Nanofabrication using a stencil mask, *Appl. Phys. Lett.* 75 (1999) 1631–1633.
- [40] Y.M. Bahk, H.R. Park, K.J. Ahn, H.S. Kim, Y.H. Ahn, D.-S. Kim, et al., Anomalous band formation in arrays of terahertz nanoresonators, *Phys. Rev. Lett.* 106 (2011), 013902.
- [41] F.G. García-Vidal, E. Moreno, J.A. Porto, L. Martín-Moreno, Transmission of light through a single rectangular hole, *Phys. Rev. Lett.* 95 (2005), 103901.
- [42] H.R. Park, S.M. Koo, O.K. Suwal, Y.M. Park, J.S. Kyoung, M.A. Seo, et al., Resonance behavior of single ultrathin slot antennas on finite dielectric substrates in terahertz regime, *Appl. Phys. Lett.* 96 (2010), 211109.
- [43] P. Weis, J.L. Garcia-Pomar, M. Höb, B. Reinhard, A. Brodyanski, M. Rahm, Spectrally wide-band terahertz wave modulator based on optically tuned graphene, *ACS Nano* 6 (2012) 9118–9124.
- [44] D. Rodrigo, O. Limaj, D. Janner, D. Etezadi, F.J. García de Abajo, V. Pruneri, et al., Mid-infrared plasmonic biosensing with graphene, *Science* 349 (2015) 165–168.